Invited Paper

Designing Nanostructures by Glancing Angle Deposition

Y.-P. Zhao*[a], D.-X. Ye[b], G.-C. Wang[b], and T.-M. Lu[b]
[a]Department of Physics and Astronomy, University of Georgia, Athens, GA 30602-2451
[b]Dept. of Phys., Appl. Phys., and Astron., Rensselaer Polytechnic Institute, Troy, NY, 12180-3590

ABSTRACT

Three-dimensional nanostructures can be fabricated by the glancing angle deposition technique. By rotating the substrate in both polar and azimuthal directions, one can fabricate desired nanostructures, such as nanorod arrays with different shapes, nanospring arrays, and even multilayer nanostructures. This method offers a fully three-dimensional control of the nanostructure with additional capability of self-alignment. There is almost no limitation on materials that can be fabricated into desired nanostructures. In this presentation, we will discuss the current status of the glancing angle deposition technology, its potential applications, and its future challenges.

Keywords: Nanostructures, nanorods, glancing angle deposition, sculptured thin film

1. INTRODUCTION

One dimensional (1D) nanowires or nanorods are anisotropic nanostructures with large aspect ratio (length/diameter), with diameters of 1 – 200 nanometers and length up to several tens micrometers. They are nanoscale building blocks in nanoelectronics, photonics, and bioengineering, and have stimulated great research interest [1-5]. Many unique and fascinating properties have already been demonstrated, such as superior mechanical toughness [6], higher luminescence efficiency [7], enhancement of thermoelectric figure of merit [8] and lowered lasing threshold [9]. Homogeneous nanowires and nanowire networks have been previously used as chemical sensors [10], field-effect transistors and inverters [11], photodetectors [12], light-emitting diodes and lasers [7, 13], and logic gates [14-18]. Very recently, by alternating the compositions of the nanostructures during fabrication, a so-called "superlattice" nanowire has been demonstrated which can greatly increase the versatility and application of these building blocks in nanoscale electronic, photonic, and biological applications [19-23]. Possible applications, including thermoelectrics, nanobarcodes, injection lasers, and one-dimensional waveguides, could be implemented through these superlattice nanostructure building blocks. One very important issue associated with these studies is how to assemble the 1D nanostructures in an effective and controllable way [24 - 26]. So far, there are four general approaches that have been employed to fabricate nanowire/nanorod structures: nanolithography-based methods, solution-based approaches, vapor-based methods, and template-based methods.

The nanolithography-based method is a widely used technique in the fabrication of 1D nanostructures [27 - 29]. It employs advanced lithographic techniques, such as electron beam lithography, x-ray lithography, or proximal probe lithography [30] with deposition and plasma etching processes. Most 1D nanostructures fabricated by nanolithography are planar structures. However, this procedure is slow and expensive, and the aspect ratio of the vertical nanorods is limited by the etching process. Currently it is not suitable for large scale fabrication of 1D nanostructures.

The solution-based approach employs controlled wet chemical reactions to synthesis nanostructures [24, 26, 31, 32]. One of the most popular solution-based approaches is solvothermal chemical synthesis [26, 32]. In this process, a mixed solvent with a certain metal precursor and a possible crystal growth regulating or template agent, such as amines, is placed in an autoclave at a relatively high temperature and pressure. Crystal growth and assembly will occur under the right reaction conditions. A drawback to this process is that it is very complicated and requires a detailed understanding of the chemical reaction and crystal growth mechanism. The products are usually not pure, and the monodispersity of the sample is far from ideal.

Vapor-based methods generally consist of vapor transport or vapor reactions at suitable temperature and pressure [24, 33]. One famous vapor-based method is vapor-liquid-solid (VLS) growth, which has been applied for whisker growth during the 1960s [34]. This method employs a catalyst to promote the anisotropic crystal growth, and a large number of materials have been grown into nanowire/rod form based upon this process. In general, a specific catalyst must be chosen for each material, and the growth temperature is usually relatively high.

Template-based methods in general use anisotropic nanoporous materials, such as anodized alumina, track-etched polycarbonate membranes, block co-polymer membranes, etc., to serve as hosts. The nanochannels in the hosts may be filled using solutions, sol-gel, or vapor, to generate the desired 1D nanowires/rods. The products may be released from the templates by selectively removing the host matrix [35-37].

Many different materials have been fabricated into nanowire/rod form based upon the processes mentioned above. Most pure elements, especially metals and semiconductors, as well as some binary materials, such as compound semiconductors and oxides, have already been fabricated into 1D nanowire/rod structures. However, in terms of material varieties, and the control of fabrication, there are still many challenges that present methods (except the nanolithography-based method) cannot meet:

(1) *There is still no general methodology to prepare 1D nanostructures from different materials, which makes the fabrication of hetero-nanostructure very difficult.* The success of semiconductor integrated circuits has shown that heterostructures with well-defined crystalline interfaces are essential in developing useful functional devices. It is arguable that the further development of 1D heterostructures (nanowires) is very important for future applications of nanoelectronics. Despite the recent excitement in heterostructure fabrication [19-23], due to the limitations of these methods, the variety of the materials one can access is inherently limited by the growth mechanisms of the preparation process. Therefore, developing a versatile and reliable nanostructure fabrication technique that is suitable for most materials is essential.

(2) *None of the above techniques is sophisticated enough to manipulate the diameters, orientations, and positions of the grown nanowires/rods.* The controls of growth are critical for future large-scale nanodevices and interconnect applications. Recently, a great deal of research has been devoted in this direction [4, 5]. Although a number of novel nanodevices based on 1D nanostructures have been realized and studied, the fabrication processes involved are usually either very complicated, or successful largely due to luck. The yields are low, and the properties of devices fabricated by the same method are not guaranteed to be identical. So far, there is no general or reliable method for fabricating large-scale nanodevices.

Recently, it has been shown that, by combining oblique angle deposition and substrate positional control, a technique called glancing angle deposition (GLAD), one can produce different nano-sized columnar films with controlled porosity and shapes [38-54]. GLAD is a physical vapor deposition process where the deposition flux is incident onto a substrate with a large angle with respect to the surface normal and the substrate is rotating. GLAD produces columnar structures through the effect of shadowing during film growth, while the substrate rotation controls the shape of the columns. During GLAD, the deposition rate not only has a vertical component (with respect to the substrate surface), but also has a lateral component. The lateral growth rate contributes to the shadowing effect, which gives rise to two major advantages for GLAD: the self-alignment effect and the lateral sculpturing effect. In this technique, there are three parameters that determine the morphology of the columns: the incident angle, the growth rate, and the substrate rotational speed. By changing the angle of incidence, the columns can be sculptured into a C-shape, S-shape, and zigzag shape, while by changing the ratio of the deposition rate to the rotational rate (which is defined as the pitch, p), the column morphology can be varied between matchstick, helical, and vertical columns [44, 45]. Since GLAD is a physical vapor deposition technique, it has many advantages in terms of controlling the growth of nanostructured thin films: 1. It can form nano-column array naturally. 2. The porosity of the film can be controlled by simply changing the incident angle. 3. There is almost no restriction on materials since the growth process is a thermal evaporation. 4. The shape and in-plane alignment of columns can be easily modified. 5. It has the advantage of self-alignment due to the shadowing effect. 6. It can also generate three-dimensional nanostructures. These advantages make the GLAD technique very promising for nanostructure fabrications. In the following, we will give a brief review on the GLAD technique.

2. NANOSTRUCTURE FABRICATION

2.1 Oblique angle deposition of columnar structured thin films

The glancing angle deposition (GLAD) technique is the extension of the commonly used oblique angle deposition (OAD) in thin film deposition community which has been practiced for many years. Most of its fundamental growth mechanisms are similar to the oblique angle deposition, although deviation may be expected. In this section we review the oblique angle deposition.

The experimental setup for oblique angle deposition is very simple, shown in Fig.1(a). The collimated evaporation beam (in ideal case) has a large incident angle θ with respect to the substrate surface normal. Therefore, we

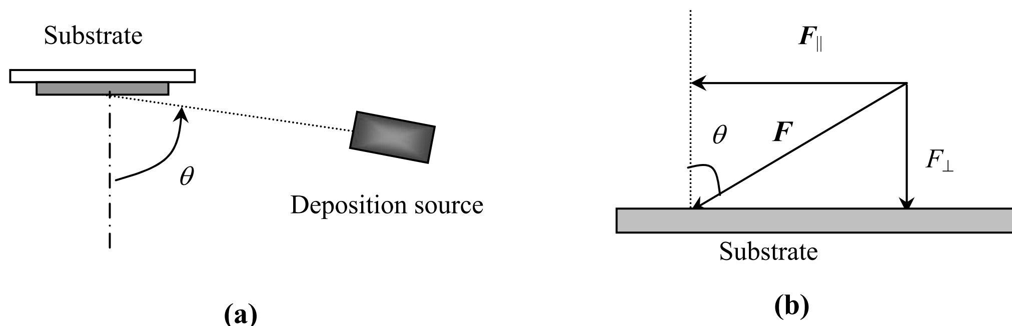

Fig. 1 (a) Experimental setup for oblique angle deposition; (b) The incident flux $\boldsymbol{F}$ can be decomposed into two different components, $F_{\perp}$ is the flux perpendicular to substrate, and $F_{||}$ is the flux parallel to the substrate.

can treat the incoming vapor flux as a vector $\boldsymbol{F}$ as shown in Fig. 1(b). The flux has two components, a vertical component $F_{\perp} = F\cos\theta$ and a lateral component (a vector) $\boldsymbol{F}_{||}$, with $|\boldsymbol{F}_{||}| = F\sin\theta$. The substrate will receive the vapor flux from both the vertical and lateral directions. During the deposition of thin film onto a flat substrate, initially the impinging atoms will randomly form islands on the substrate as shown in Fig. 2(a). As deposition proceeds, the initial nucleated islands will act as shadowing centers, and all the tallest islands will receive more impinging atoms as compared to the shorter ones (shadowing effect). This competition process will only leave the tallest islands grow into columns, and a nanocolumnar film will be formed. Clearly, the lateral component $\boldsymbol{F}_{||}$ is the source for the shadowing effect. For the oblique angle deposition, since $\boldsymbol{F}_{||}$ remains constant during deposition, a columnar film with tilt angle β will be formed. Figure 3 shows the cross-sectional SEM pictures of Si thin films deposited at different incident angles: at $\theta = 0^{o}$, a continuous and uniform thin film is formed; at $\theta = 30^{o}$, small columns began to grow; at $\theta = 60^{o}$, the columnar structure becomes more obvious; at $\theta = 80^{o}$, the obvious columnar structures are formed in the film. In general, the column tilt angle β is less than the vapor incident angle θ, and follows the empirical tangent rule, $\tan\beta = 1/2 \tan\theta$ for small θ [55, 56], or the cosine rule, $\beta = \theta - \arcsin(\frac{1-\cos\theta}{2})$ [57].

Clearly, thin films deposited by oblique angle deposition have the following characteristics: The films are in general porous, possessing nano-columnar structures. The nanocolumns are tilting away from the surface normal to the incident evaporation beam direction. The size and density of the nanocolumns change as function of the incident angle θ.

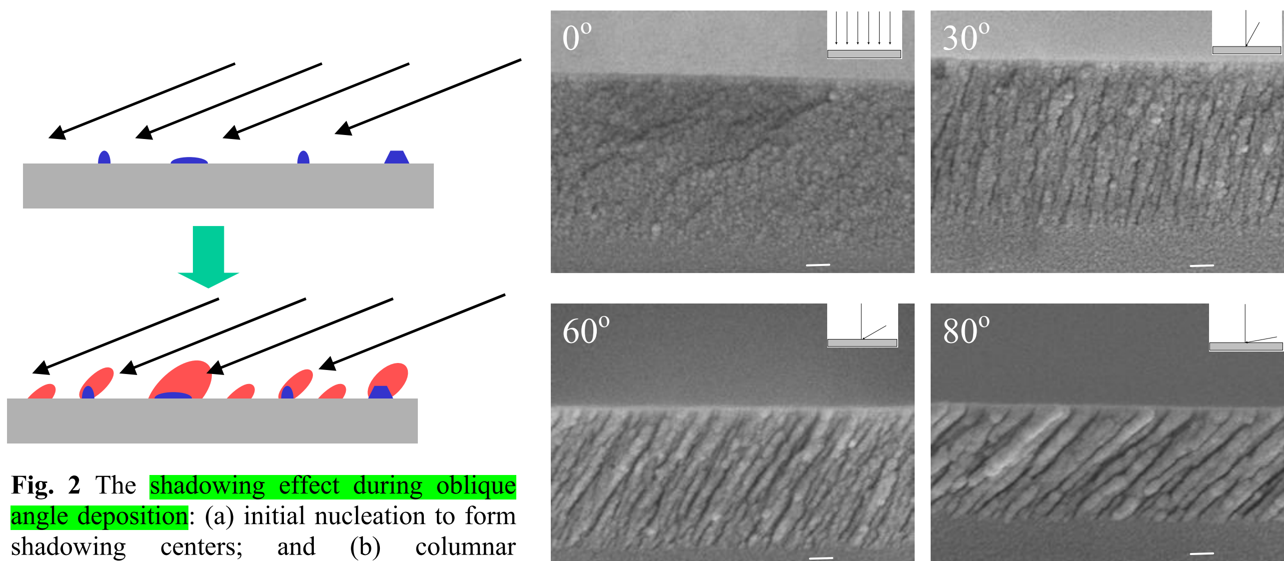

Fig. 2 The shadowing effect during oblique angle deposition: (a) initial nucleation to form shadowing centers; and (b) columnar structures formed due to the shadowing effect.

Fig. 3 SEM cross section view of Si films fabricated at different incident angles. The scale bar is 100 nm.

2.2 Glancing angle deposition (GLAD)

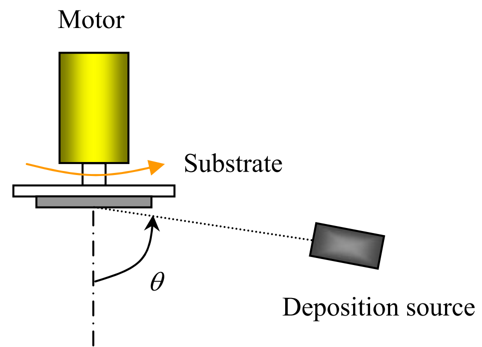

Fig. 4 Experimental setup for GLAD.

Although the nanocolumnar films generated by the oblique angle deposition can be treated as one kind of nanostructures, the structures are not easy to control during the growth. The preferred tilting columnar angle β introduces anisotropy in the films, which, in most cases, are not desirable. In order to better control the orientation as well as the structure of the nanocolumns, the glancing angle deposition technique is developed based on the oblique angle deposition, as shown in Fig. 4. The basic deposition setup is exactly the same as that of the oblique angle deposition, the only difference is that the substrate is manipulated by two stepper motors, one motor controls the incident angle θ, another motor controls the azimuthal rotation of the substrate with respect to substrate surface normal. During the deposition, the substrate can rotate azimuthally at a fixed incident angle, or rotate back and force changing the incident angle, or rotate azimuthally and polarly simultaneously. The movements of the two motors are controlled by a computer. By changing the speed and phase of the azimuthal rotation, polar rotation, the combination of the two rotations, as well as the deposition rate, the nanocolumns can be sculptured into a C-shape, S-shape, and zigzag shape, or matchstick, helical, and vertical columns [38-54]. The following sections will give examples of various Si nanostructures fabricated in such a way. The general experimental conditions are the following: the experiments were performed in a high vacuum chamber with a background pressure of 2×10^{-4} Pa. The Si (99.9995%, from Alfa Aeser) was evaporated by an electron beam bombardment method or the e-beam evaporation method. The pressure during deposition was less than 1×10^{-3} Pa, and the growth rate was monitored by a quartz crystal microbalance. The stepper motor was attached to a water-cooled stand and the circulating chilling water was held at 4°C. The chilling water prevents the warming up of the sample. The distance between the evaporation source and the substrate was about 30 cm. During the deposition, the deposition rate was fixed, while the rotation speed was controlled by a computer.

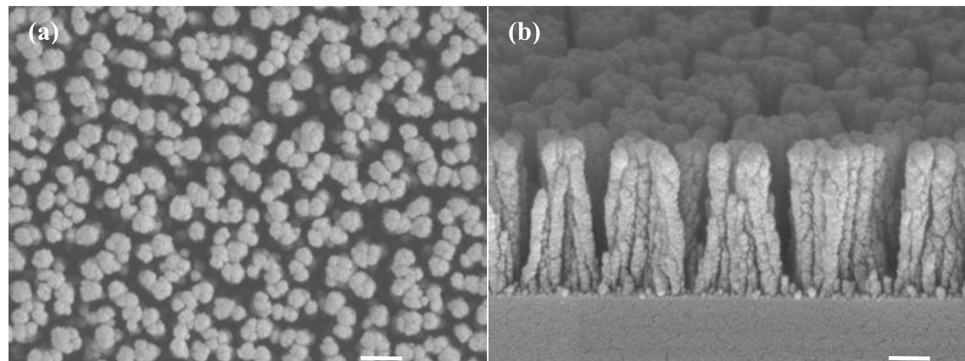

Fig. 5 Vertically aligned nanocolumnar structures: (a) SEM top view; and (b) SEM cross-sectional view. The scale bar is 200 nm.

2.3 Growth of vertically aligned nanorod arrays

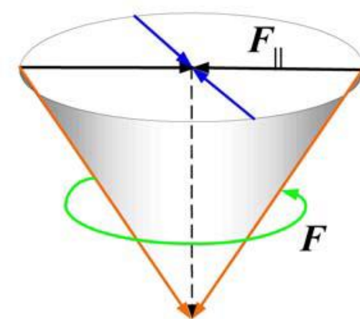

Fig. 6 Cancellation of the $F_{\|}$ term due to the rotation. Effectively, only F⊥ contributes effectively to the increasing height of the nanocolumns.

The simplest aligned nanostructures GLAD can produce are the vertical aligned nanorod structures. By fixing the incident angle at relatively glancing (> 75°), and continuously rotating the substrate azimuthally with a suitable constant speed, vertically aligned nanocolumns can be formed. Figures 5 (a) and (b) show an example of the nanocolumnar structure deposited with a rotation speed of 0.0019 rev/s, and total 100 substrate revolutions. The incident angle of Si vapor flux with respect to the rotating substrate surface normal was fixed at 85°. The growth rate R was 0.2 nm/s. The nanocolumns are all aligned vertically respect to the substrate, and the location of the columns are random as revealed by the top view and side view of SEM images (Fig. 5).

The formations of the vertical aligned nanocolumns are expected if we consider the direction of the flux as shown in Fig. 1(b). Since the substrate rotates azimuthally, each part of the surface has an equal chance to receive the same amount of particles from the $\boldsymbol{F}_{||}$ component. After a complete revolution, the average $\Sigma\boldsymbol{F}_{||}$ is zero due to the cancellation of $\boldsymbol{F}_{||}$ at opposite directions, which means there is no preferred orientation of the nanocolumn as shown in Fig. 6. Effectively there is only vertical growth and the vertically aligned columns are formed. The effective $F_{||}$ is zero, while the effective $F_{\perp}$ is a constant. Clearly the purpose of the azimuthal rotation is to constantly adjust the column tilting direction to make them straight.

2.4 Growth of helical nanostructures

If the substrate rotation speed is intentionally slow down compared to the deposition rate, since at each rotation interval, there will be enough amount of particles deposited onto the substrate to form a preferred orientated column, the result of this slow continuous rotation gives a continuous formation of nanocolumns along different direction. Thus, helical nanorod will be formed in such a way. By controlling the time interval between each rotation step, as well as the incident angle, one can control the length, diameter of the pitch, the diameter of the rod, and the number of turns of the helical nanorod structure. The following gives a special example of fabricating spiral square nanocolumns.

To fabricate square spiral posts (or square spirals) with a circumference of L for one pitch, we fix the flux incident angle at 85° and program the stepper motor with the following sequence: 1. Grow a layer with thickness of $L/8$ without rotating the substrate. 2. Rotate 90° at a fast rotation rate (0.05 rev/s). 3. Repeat steps 1 and 2. 4. Grow a layer with thickness of $L/4$ without rotating the substrate. 5. Rotate 90° at a fast rotation rate (0.05 rev/s). 6. Repeat steps 4 and 5 to the desired pitch number for the square spirals. The expected square spiral structure is shown in Fig. 7.

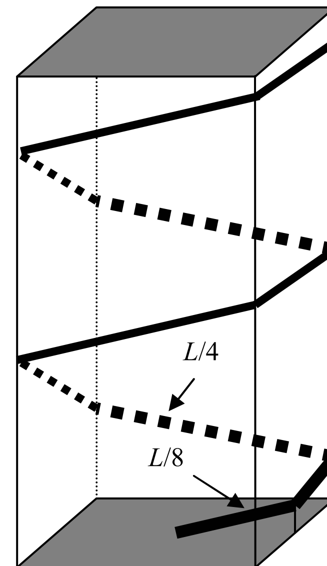

Fig. 7 The sequence for fabricating a 2-turn square spiral. At the fixed flux incident angle, the stepper motor is programmed with the following sequence: 1. Grow a layer with thickness of $L/8$ without rotating the substrate. 2. Rotate 90° at a fast rotation rate. 3. Repeat steps 1 and 2. 4. Grow a layer with thickness of $L/4$ without rotating the substrate. 5. Rotate 90° at a fast rotation rate. 6. Repeat steps 4 and 5 to the desired pitch number for the square spirals. In this case, the total number of pitch is 2.

The fabricated square spiral arrays on bare Si substrates are shown in Fig. 8. Both the top-view and cross-sectional SEM images show that the spirals are uniformly distributed across the whole surface with almost the same length. However, each spiral is closely packed to the adjacent spiral, which means that the whole film should act as a spiral bed instead of individual spirals. The spiral structure of the spiral is described by the arrows in Fig. 8b. From the substrate to the top of the spiral, the arrow changes direction 10 times: the first two direction changes are small, which correspond to the $L/8$ arms, and the remaining eight turns correspond to the

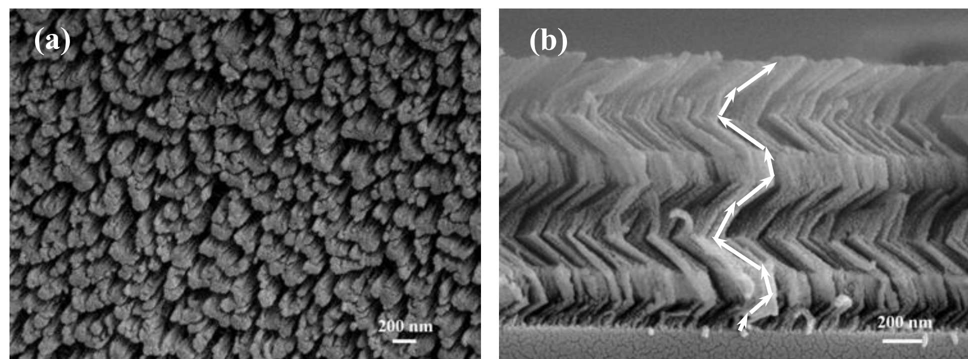

Fig. 8 SEM images of 2-turn square Si spirals. (a): top-view and (b): cross-section of Si spirals on a bare Si substrate. The arrows on (b) indicate the growth sequence in a spiral, which is similar to what we expect in Fig. 7. The spirals are uniformly distributed across the whole surface with almost the same length, and each spiral is closely packed to the adjacent spiral with the diameter of the Si arm about 50 nm.

8 $L/4$ arms, which represent two complete turns of the square spiral. This structure is similar to what we expect in Fig. 7. The diameter of the Si arm is about 50 nm, and the diameter of the spiral is about 200 – 500 nm. The twist angle of the spiral is determined by the incident flux angle since the fabrication process is mostly under a fixed angle deposition. The resulting tilt angle (similar to the experiment shown in Fig. 3) was determined to be $55^{o} \pm 2^{o}$.

By adjusting the parameter of L, smaller sized spiral nanostructure can be formed. Figure 9 shows a 10-turn spiral film. The deposition conditions are almost exactly as the previous one except L = 200 nm.

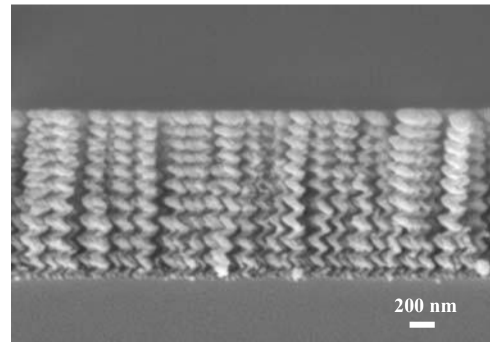

Fig. 9 SEM cross-sectional image of 10-turn square Si spirals.

2.5 Integration of multilayered nanorod structures

Since different azimuthal rotation speed (or direction) gives different topography of the nanocolumns, by programming the stepper motor with different speeds (or directions) in different growth periods, we can build a multilayered nanostructure with different topography. Figure 10 shows one example of the multilayer square spiral/straight nanocolumns. To fabricate the multilayer square spiral/straight nanocolumns, we first fabricated the spiral arrays to a preset pitch, then continuously rotate the substrate in a faster speed to build up the thickness of straight nanocolumns to be the same as the spiral. We then repeat the whole process again. For the film deposited in Fig. 10, the growth conditions are, R = 0.32 nm/s, L = 120 nm, and the rotational speed for the column is 0.0019 rev/s.

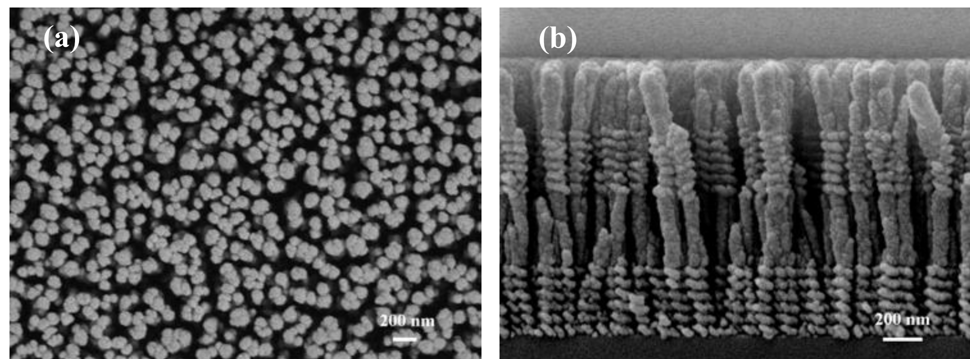

Fig. 10 SEM (a) top-view and (b) cross-section images of multilayer Si spiral/straight nancolumns grown on a bare Si(100) substrate. There are two layers of 6-turn spirals and two layers of 300-nm long columns.

There are two layers of 6-turn spirals and two layers of 300-nm long columns. The two spiral sections and two column sections are almost the same. Unlike the spirals shown in Fig. 8(b), it appears that the initial square spirals are separated and each rod is sitting on an individual spiral. The fine structure of the multilayer columns is investigated by TEM as shown in Fig. 11. This sample was taken from the same Si substrate, and the arrow indicates the column growth direction. Unlike the SEM image shown in Fig. 10(b), the TEM image shows a dramatic difference between the two spiral sections. For the initial grown spiral section, it consists of a large number of fine spirals overlapping with each other. During the first section of column growth, the nearest neighbor spirals seem to group together and form nucleation sites for column growth. However, the second spiral section has individual spirals with large rod diameter. This is because after the first section of column growth, the grown columns act as the

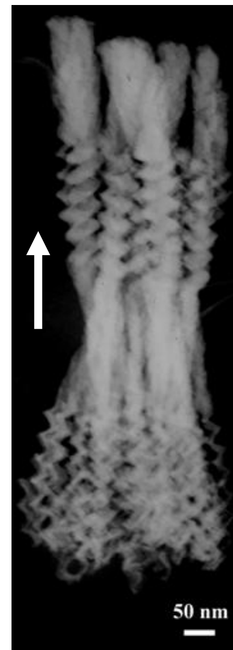

Fig. 11 TEM image of a bundle of multilayer spiral/column rods grown on a Si substrate. The arrow on the image shows the growth direction. A dramatic difference between the two spiral sections can be seen. For the initial grown spiral section, it consists of a large number of fine spirals overlapping with each other, while the second spiral section has individual spirals with much larger rod diameter.

nucleation centers for the second spiral growth. Those nucleation centers are similar to the colloid substrate case we have discussed, and the diameter of the column and the incident angle of the flux determine the diameter of the Si rod for the spiral. Thus, the TEM shows that the rod diameters of the second spirals follow the diameters of the Si rods underneath.

Clearly by changing the computer program in a similar manner, other kinds of multilayered nanostructures can be fabricated.

2.6 Phase modulation: controlling the shape of the nanorods

For above mentioned nanostructure fabrication, we have only utilized one parameter of the rotation, i.e., the speed of the rotation. However, another very important parameter for a rotation is the phase. For the rotation with only one speed, the phase almost has no effect of the nanostructure formation. However, if we introduce two different rotation speeds during one evolution, then the relative phase difference between these two rotation speeds becomes very important, and can be used to tune topology of the nanostructures (in fact, the fabrication of the square spirals can be also treated as one of this case). One obvious way to incorporate the phase factor is to introduce symmetric rotation with two different rotation speeds.

In order to do so, we divided each revolution during deposition into $2N$ sectors, where N represents the symmetry of the desired shape of the columns. The motor speed was alternatively changed between $R_l = 0.00187$ rev/s and $R_h = 0.05$ rev/s for adjacent sectors. Since R_h is almost 30 times higher than R_l, the pitch p_h is almost 30 times lower than p_l. Therefore, within the sector with rotational speed R_h, the sample will receive almost 30 times less amount of Si vapor per radian than that with R_l. In our experiments, the sectors were not evenly divided. In fact, the angular sector size for R_l was fixed at 22.5^o, while the sector size for R_h changed with the desired symmetry of the columns. For example, if a two-fold symmetric column is desired, the angular section size for R_h is 67.5^o, while for a four-fold symmetric column, the R_h section size is 22.5^o, and so on.

Figure 12 shows the scanning electron microscopy (SEM) top-view images of the samples (sample numbers are the same as figure labels). Column I contains the SEM images of the samples deposited on bare Si(100) substrates while Column II contains the images from those of the colloid substrates. Column III contains the polar plots of the pitch number ($p_l > p_h$, only for illustration purpose) for each revolution, which also reveals the symmetry of the desired columns. Under all these conditions, vertical columns (as shown in Figure 13) are formed despite the different rotation schemes. The diameter of the columns is less than 80 nm. For films deposited on bare Si(100) substrates (column I), Sample (A) has conventional circular columns with a single rotation rate R_l. There is no preferred direction of alignment for the columns, and the columns seem to aggregate together (Fig. 13 (A)). Sample (B) has a two-fold symmetry, and each individual column has an elliptical shape (see the white oval in Fig. 12 (IB)). All the columns seem to align along one principal direction (the white arrow in Fig. 12 (IB)), and they tend to aggregate like walls along one direction (Fig. 13 (B)). Sample (C) has three-fold symmetry, and the column tends to form triangular shape. Although the columns seem to build up randomly, they are more or less aligned along three principal axes as highlighted by the white arrows in Fig. 12 (IC). From the cross-sections it appears that the columns of sample (C) distribute more evenly than (A) and (B) (Fig. 13(C)). The four-fold symmetric sample (D) forms rectangular shaped columns, and the columns are aligned along two principal axes. The cross-section of the columns in sample (D) looks similar to that of sample (C) (Fig. 13(D)). However, for the five-fold symmetric sample (E), one can barely find any columns with a five-fold symmetry. Also, the principal axes of alignment are not very clear. Figure 12 (IE) is very similar to Fig. 12 (IA). One possible reason is that for the five-fold symmetry, the angular sector size for R_h is only 13.5^o, which is much smaller than 22.5^o for R_l. Also, as the symmetry becomes higher, the column shape becomes closer to the circular shape. However, we will demonstrate later that by changing the size of the initial nucleation center, we can still fabricate five-fold symmetry columns.

If one examines Fig. 12 (IB) to Fig. 12 (ID) more carefully, one finds that some columns have flower-like patterns. For example, the elliptical column has two petals, the triangular column has three petals, and the rectangular column has four petals. A zoomed-in atomic force microscope (AFM) image of the four-fold symmetric column is shown in Fig. 14. Each petal is about 100 nm in size. These nano-sized flowers and the aligned random column arrays demonstrate the ability of GLAD for lateral nanoscale engineering. We also notice from Fig. 12 that not every column has the same flower-like pattern. For example, Fig. 12(ID) shows that some columns only have three petals, and some have two. These imperfect shapes are due to the random nucleation during growth. Since the columnar films are deposited on flat Si(100) substrates, the initial nucleation happens randomly on the substrate surface. If the adjacent nucleation centers are far from each other, the further growth of columns onto these adjacent nucleation sites will not affect each other. However, if the adjacent nucleation sites are close, one site may affect (shadow) another site at specific

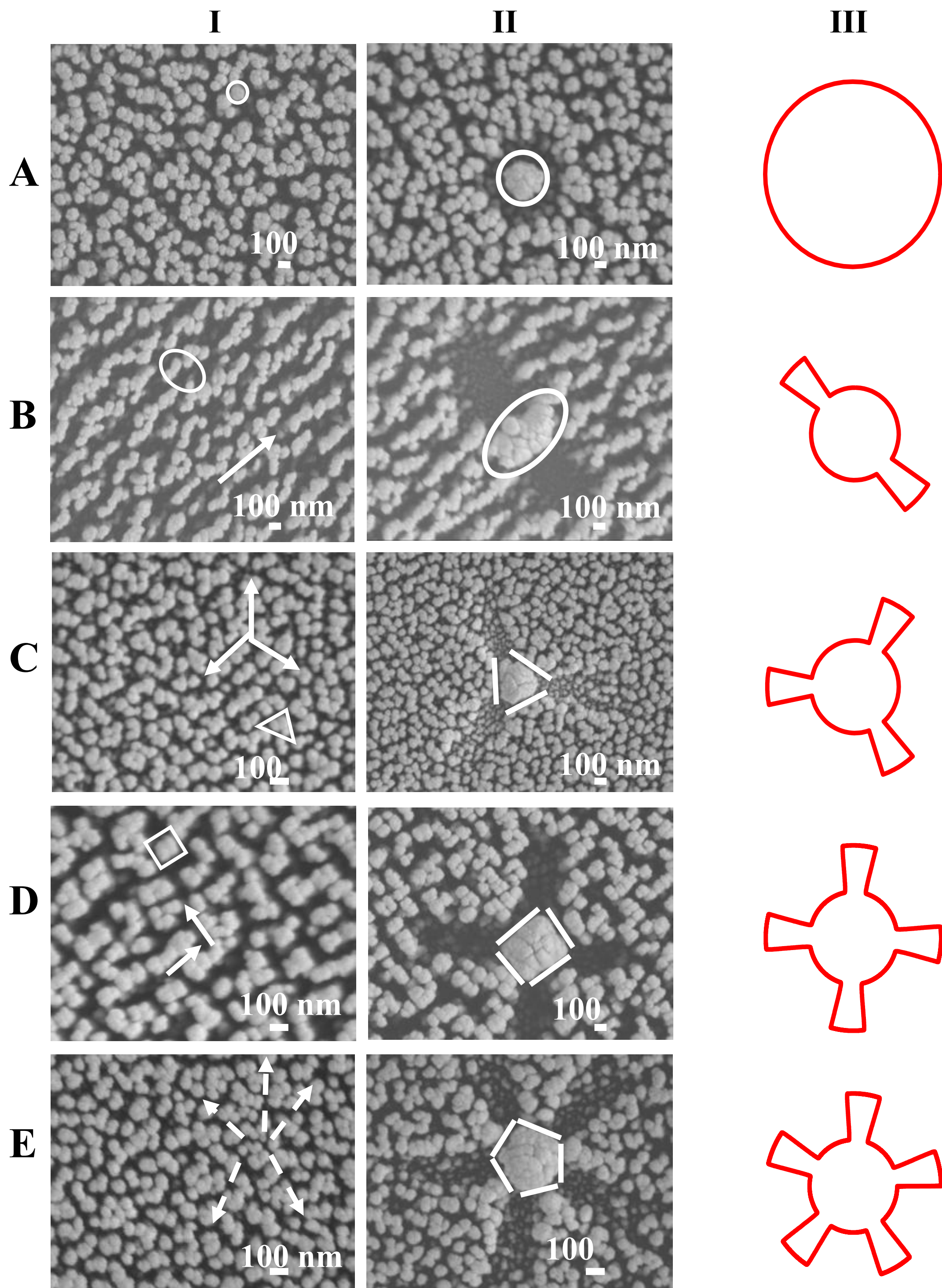

Fig. 12 SEM top view images of ten different GLAD samples with different rotational symmetries. Column I lists films deposited on bare Si(100) substrates, Column II lists films deposited on the colloid substrates which have point defects, while Column III illustrates the rotational symmetries. Sample A is obtained under a constant rotation speed. Sample B, Sample C, Sample D, and Sample E have two-fold, three-fold, four-fold, and five-fold symmetries, respectively, obtained from different rotational symmetries shown in III.

directions and columns with missing petals result. Therefore, if one can control the position of initial nucleation sites, giving them with sufficient separation, one can fabricate perfect nano-flower arrays.

The size of the nano-columns depends on the original size of the initial nucleation center. If there are larger nucleation centers on the substrate, they can form perfectly shaped columns. Figure 15 shows SEM images of films deposited on a colloid substrate. The 90 nm Polystyrene colloids tend to form a monolayer which consists of domains and depletion regions. There are colloid defects in the depletion regions as shown in Fig. 15(A). The sizes of the colloid defects vary, from one single colloid particle to aggregates of several particles. These defects serve as nucleation centers during GLAD. As shown in Fig. 15(B), for GLAD of Si with five-fold symmetry, due to the strong shadowing effect, pentagon shaped columns formed at those nucleation centers. Clearly the shape of the column is independent of the size of the initial nucleation center, while the size of the column does depend on the initial size of the nucleation center. The size appears to be proportional to the size of the nucleation center. In this case, the size of the nucleation center (> 90 nm) is larger than that of the column size (~ 80 nm) on a flat, defect free substrate. Similar phenomena have been observed (not shown) for all the rotation schemes shown in Fig. 12 (II). For the continuous rotation, the column shape is a circle (Fig. 12 (IIA). For a two-fold symmetry, three-fold symmetry, and four-fold symmetry, it is an oval (Fig. 12 (IIB)), a triangle (Fig. 12 (IIC)), and a rectangle (Fig. 12 (IID))

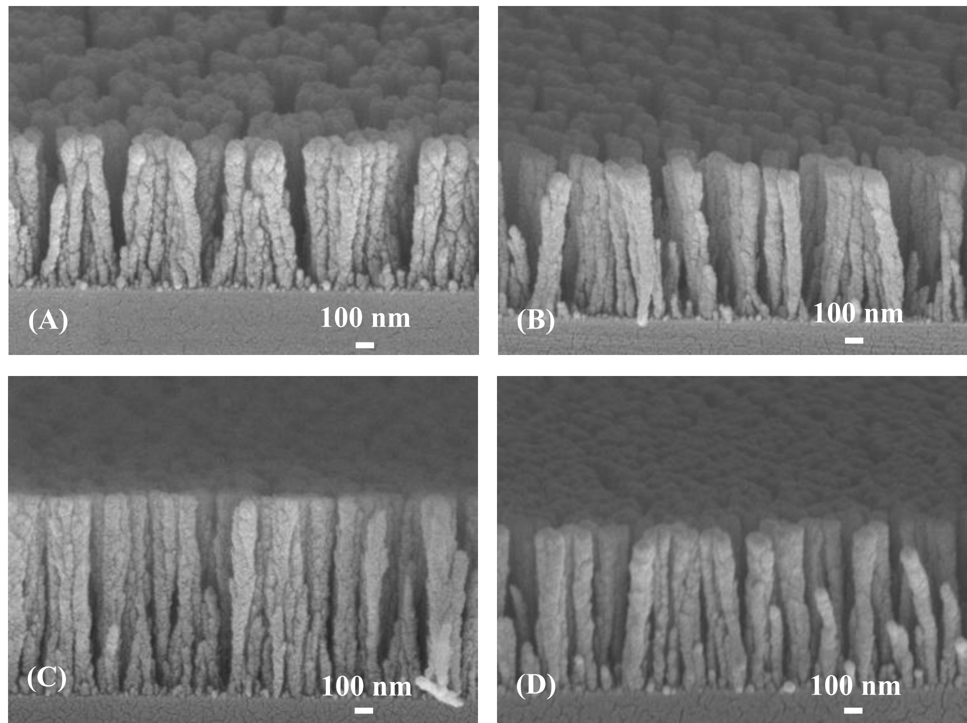

Fig. 13 Cross-sectional SEM images of Samples A to D. All deposited films consist of columns, and the size of the columns is less than 80 nm.

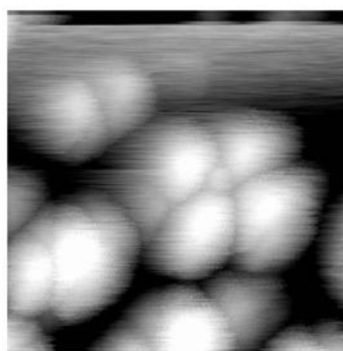

Fig. 14 A four-fold symmetric nano-flower imaged by AFM.

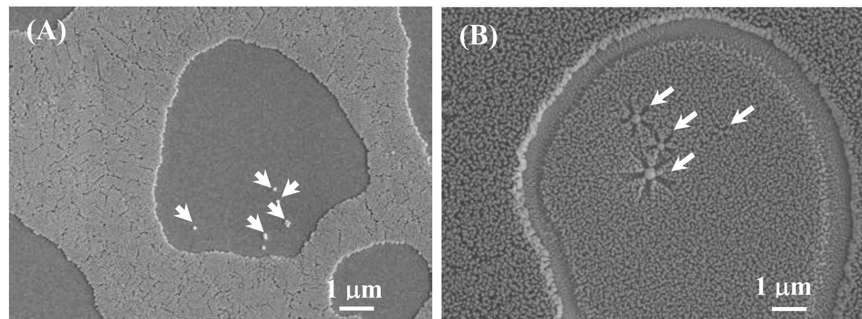

Fig. 15 The effect of initial nucleation center. (A) The SEM top-view of a colloid substrate. The surface has colloid occupied region and non-occupied region. In the non-occupied region, there are colloid defects with various sizes indicated by white arrows. (B) The SEM top-view of the Si film with a five-fold symmetry grown on a colloid substrate. At the nucleation centers, pentagonal columns are formed with different sizes proportional to the size of the initial nucleation centers.

structure, respectively. Clearly, both the shape of the column, and the shadows induced by the growth, reflect the symmetry of the deposition. Therefore by controlling the size of the nucleation center, one can either fabricate flower-like column, or columns with different shapes.

2.7 Phase modulation: controlling the orientation of the nanorods

Angular Sector

The next immediate question is, if the phase sectors are not divided symmetrically, what will happen to the nanocolumar structures? One simplest case is to divide one revolution into two different phase sectors as shown in Fig. 16. In Sector I, the substrate rotates at speed R_l for an angular range of ϕ, and in Sector II, the substrate rotates at speed R_h for an angular range of $2\pi - \phi$. We set $R_l < R_h$. Since the asymmetry in the ϕ is intentionally introduced, there will be a net $\boldsymbol{F}_{||}$ after a complete revolution, and will result in an effective vapor incident angle α different from θ. According to Fig. 16, the apparent lateral flux $F'_{||}$ will be changed according to the sizes of sectors and the ratio of the rotational speeds:

$$F'_{\parallel} = \left[\int_{-\phi/2}^{\phi/2} \frac{F_{\parallel}\cos\varphi}{R_l} d\varphi + \int_{\phi/2}^{-\phi/2} \frac{F_{\parallel}\cos\varphi}{R_h} d\varphi \right] / t = \frac{2F_{\parallel}}{t}\left(\frac{1}{R_l} - \frac{1}{R_h} \right) \sin\frac{\phi}{2}. \tag{1}$$

The total time t for a complete revolution is

$$t = \frac{\phi}{R_l} + \frac{2\pi - \phi}{R_h}. \tag{2}$$

Therefore the effective flux incident angle α can be expressed as

$$\tan\alpha = \frac{F'_{\parallel}}{F_{\perp}} = \frac{2F\sin\theta\left(\frac{1}{R_l} - \frac{1}{R_h} \right)\sin\frac{\phi}{2}}{F\cos\theta\left(\frac{\phi}{R_l} + \frac{2\pi - \phi}{R_h} \right)} = 2\tan\theta\sin\frac{\phi}{2}\frac{\left(\frac{R_h}{R_l} - 1 \right)}{2\pi + \left(\frac{R_h}{R_l} - 1 \right)\phi}. \tag{3}$$

Since the experimental incident angle θ is fixed, the density of the column should be a constant; while the effective incident angle α is changed with ϕ and R_h/R_l, we expect the tilt angle β will change. A special case is if the substrate is rotated uniformly, $\omega_2/\omega_1 = 1$, then $\tan\alpha = 0$. The deposited columns have no preferential deposition angle, and the columns stand up along the normal of a substrate.

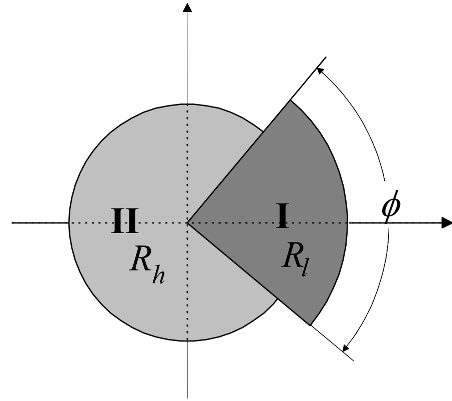

Fig. 16 Substrate rotational pace in one revolution. The first angular sector ϕ rotates at speed ω_1 and the rest sector with speed ω_2.

We have used this method to grow Co films on Si(100) substrates. Cobalt slugs (99.95%, from Alfa Aeser) placed in an Al_2O_3 crucible were thermally evaporated by a current passing tungsten basket and the incident angle θ was fixed to be 65° and 75° in each run. The angular range ϕ of the phase sector was set to be either 45°, 90°, 135°, 180°, or 225°, and the rotational speed R_l is fixed at 0.0015 rev/s and R_h to be 0.0045 rev/s. Figure 17 shows the cross-sectional views of cobalt films for ϕ = 45°, 90°, 135°, and 180°, at θ = 65° and R_h/R_l = 0.0045/0.0015 = 3. The column tilt angle β increases and then decreases when ϕ changes from 45° to 135° and then to 180°. Figure 18 summarizes the tilt angle β as a function of angular sector ϕ for two incident angles, θ = 65° and 75°, at a fixed ratio of rotational speeds ω_2/ω_1 = 3. It is seen that even for a fixed incident angle, one can achieve a wide range of column tilt angle using this rotation scheme. The solid curves are the calculated effective incident angle α as a function of angular sector ϕ at θ = 65° and 75°. Although we do not expect that the calculated effective incident angle α predicted by Eq. (3) can be used to fit the data, the trends of measured β versus ϕ are consistent with the trend of predicted α. Note that the measured β is always less than the calculated α, just like β is always less than θ in the case of fixed angle deposition without rotation. The tilt angle β increases to a maximum at a critical angular sector ϕ_c around 135° and then decreases. This is consistent with Eq. (3) in which the ϕ_c satisfies the equation,

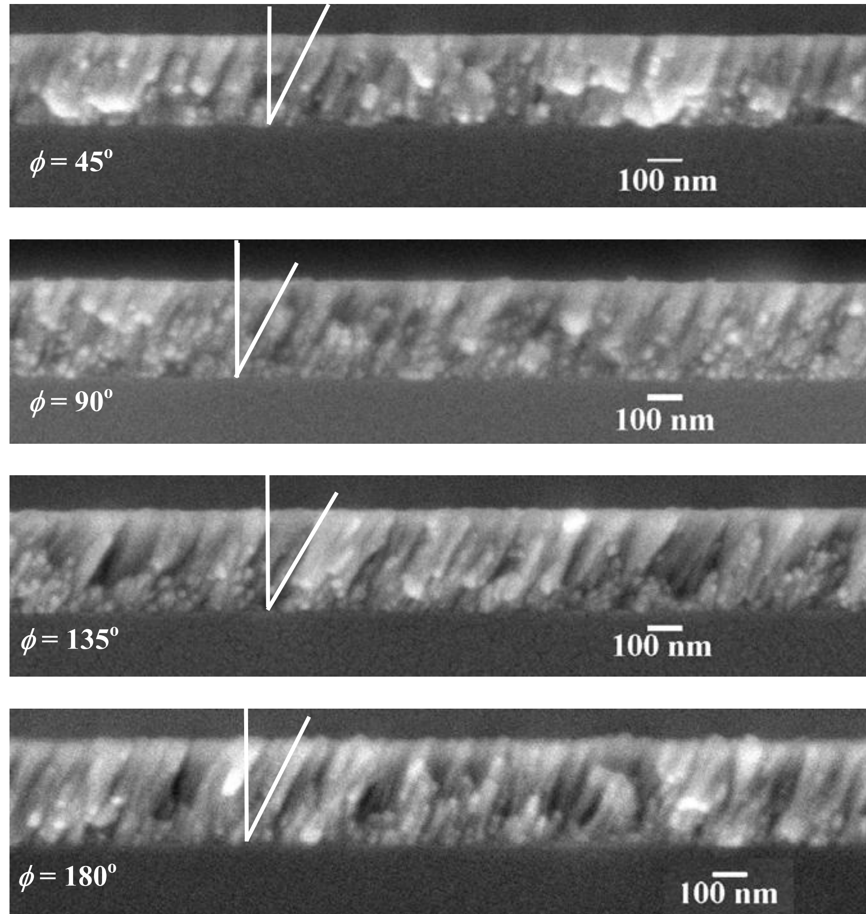

Fig. 17 SEM cross-sectional images of Co films deposited at $\theta = 65°$ and $R_h/R_l = 3$. The columns tilt to different angles β for different angular sectors ϕ. The white lines highlight the measured tilt angles. The scale bar in each image represents 100 nm.

$$2\tan\frac{\phi_c}{2} = \frac{2\pi}{R_h / R_l - 1} + \phi_c \,. \tag{4}$$

For $\dfrac{R_h}{R_l} = 3$,

$$2\tan\frac{\phi_c}{2} = \pi + \phi_c \,. \tag{5}$$

Numerically ϕ_c value is determined to be around 141°, which is consistent with the experimental result.

2.8 Formation of regular array of nanorods by templates

Almost all the nanocolumnar films shown above (except for Fig. 15) are deposited onto flat bare Si substrates, in which cases the random nucleation is the deterministic mechanism for the lateral distribution of the nanocolumns. However, if we can use one of the major growth mechanisms of GLAD, the shadowing effect, properly, we can grow high aspect ratio regular array of nanocolumns. To achieve this goal, we can use a substrate with proper two-dimensional nano-template. The features on the template will act as shadowing centers, and the deposition particles will only accumulate onto the shadowing centers under the proper geometric deposition condition. For examples, Fig. 19 shows

the nanocolumns grown on colloid substrates with particle size of 89 nm. The monolayer of Polystyrene colloid substrate was prepared on a Si(100) substrate by the method suggested by Micheletto et. al. [58]. Figure 19(a) shows the colloid substrate, which possesses a close-packed hexagonal structure. Figure 19(b) shows the cross-section of the nanocolumns grown onto the colloid substrate. The growth conditions were exactly the same as that of Section 2.3. The cross-sectional view shows that almost each nanocolumn sits on a colloid particle, which means that the colloid particles have successfully served as nucleation centers.

We can also use other technique to prepare template, for example, microfabrication process or other nanolithography methods such as e-beam lithography, SPM lithography, etc. Figure 20 shows an example of regular helical Si spring grown onto regular W plugs fabricated by photolithography method. Clearly, the use of template provides a lateral control of the nanocolumn growth.

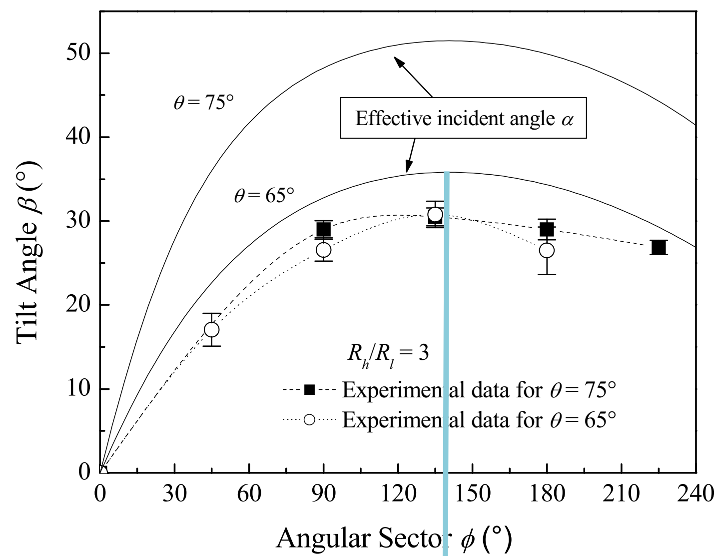

Fig. 18 Measured tilt angle β vs angular sector ϕ for R_h/R_l = 3 and θ = 65° (○) and θ = 75°(■). The solid curves are the effective incident angles α predicted by Eq. (3) for the same growth conditions.

2.9 Control film porosity

All above fabrication methods only concentrates on one degree of freedom of the substrate manipulation: azimuthal rotation. In fact, there are two other rotation degrees of freedom one can utilize: the polar rotation to change the particle incident angle θ, and the nutation to rotate the substrate to facing different phase of the incident flux. The polar rotation has been demonstrated to change the size and density of the nanocolumns as shown in Fig. 3, while the nutation has not been used for nanocolumn fabrication.

In principle, one can control all the three degrees of freedom for rotation to fabricate desired nanostructures.

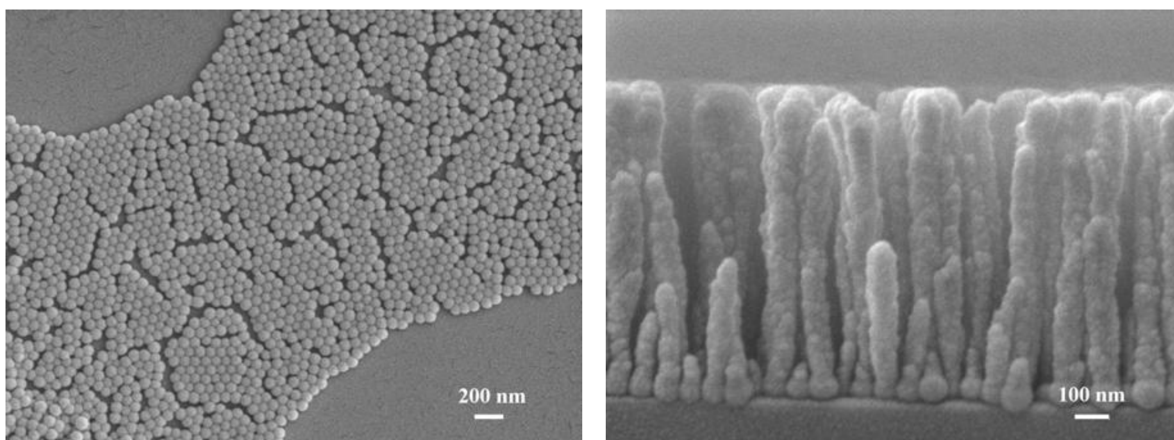

Fig. 19 (a) Top-view SEM images of colloid substrates with colloid particle diameter of 89 nm; (b) cross-section of Si nanocolumns on 89 nm colloid substrate. The columns form a certain regular pattern on the surface and almost each nano-column (with size ~ 40 nm – 70 nm) sits exactly on a colloid particle.

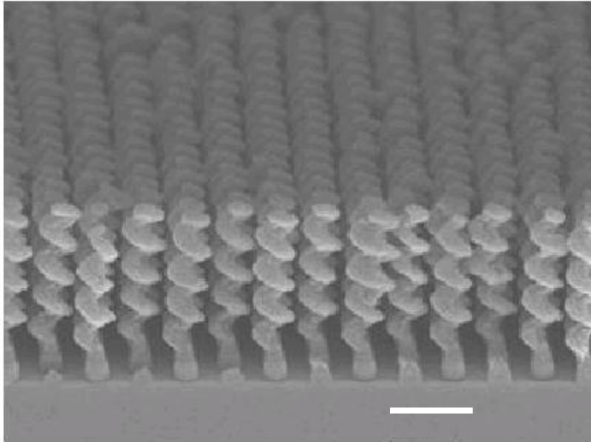

Fig. 20 SEM side view of regular helical Si spring grown onto regular W plugs fabricated by photolithography method. The scale bar is 1 μm.

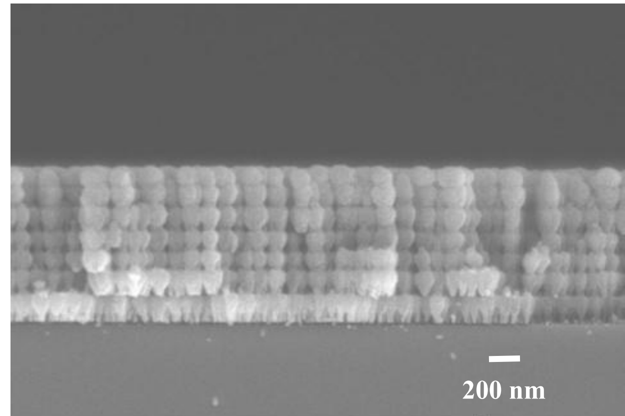

Fig. 21 SEM cross-sectional view of three-dimensional porous Si structure fabricated by combining azimuthal and polar rotations.

Figure 21 shows an example of a porous Si thin film fabricated by combining azimuthal rotation and polar rotation. To fabricate this film, the sequence of the deposition is the following: (1) Open shutter; (2) set θ = 85º, and deposit for 200s; (3) change θ to 75º, and deposit for 100s; (4) change angle θ to 20 º , and deposit for 100s; (5) Close shutter; (6) change angle θ from 20º to 85º; (7) repeat 1-6 steps for another 6 times (7 layers). During the deposition, the azimuthal rotation was preceded with a rotation speed of 0.5 rev/s, and the deposition rate was 0.5 nm/s.

3. CONCLUSIONS

We use above examples to demonstrate that the GLAD technique has the following advantages in terms of fabricating nanostructures: (1) It can form vertical aligned nanorod array naturally. This is superior to most of the conventional CVD or VLS methods, where a great deal of effort has been made to fabricate aligned nanowires. (2) The size and density of the nanorods can be controlled by the vapor incident angle. (3) There is virtually no materials limit. As long as the material can be evaporated, it can form vertical aligned nanorod structures. (4) The shape, alignment, and orientation of the nanorods can be easily changed by programming the rotation procedures. (5) The shadowing effect introduces a self-alignment effect, where templates can be used to mediate the size and orientation of nanorods; (6) Three-dimensional shaped nanorod structures can be sculptured by computer programming. In fact, the most intriguing fact of GLAD is that the structures of the nanorods can be well-designed in such a way. This cannot be achieved by any other nanostructure fabrication techniques.

REFERENCES

1. Y. Imry, *Introduction to mesoscopic physics*, 2nd Edition. (Oxford University Press, Oxford, 2002).
2. *Mesoscopic physics and electronics*. Edited by T. Ando, Y. Arakawa, K. Furuya, S. Komiyama, and H. Nakashima (Springer, Berlin, 1998).
3. A. P. Alivisatos, *Semiconductor clusters, nanocrystals, and quantum dots.* Science **271**, 933 (1996).
4. *WTEC panel report on nanostructure science and technology: R&D status and trends in nanoparticles, nanostructured materials, and nanodevices*. Edited by R. W. Siegel, E. Hu, and M. C. Roco (Kluwer Academic Publishers, 1999).
5. *The technology roadmap for nanoelectronics*. European Commission, 1999.
6. E. W. Wong, P. E. Sheehan, and C. M. Lieber, *Nanobeam mechanics: elasticity, strength, and toughness of nanorods and nanotubes*. Science **277**, 1971 (1997).
7. X. Duan, Y. Huang, Y. Cui, J. Wang, and C. M. Lieber, *Indium phosphide nanowires as building blocks for nanoscale electronic and optoelectronic devices*. Nature **409**, 66 (2001).

8. Z. Zhang, X. Sun, M. S. Dresselhaus, J. Y. Ying, and J. Heremans, *Electronic transport properties of single-crystal bismuth nanowire arrays.* Phys. Rev. B. **61**, 4850 (2000).
9. M. Huang, S. Mao, H. Feick, H. Yan, Y. Wu, H. Kind, E. Weber, R. Russo, and P. Yang, *Room-temperature ultraviolet nanowire nanolasers.* Science **292**, 1897 (2001).
10. F. Favier, E. C. Waiter, M. P. Zach, T. Benter, and R. M. Penner, *Hydrogen sensors and switches from electrodeposited palladium mesowire arrays*. Science **293**, 2227 (2001).
11. Y. Cui and C. M. Lieber, *Functional nanoscale electronic devices assembled using Silicon nanowire building blocks*. Science **291**, 851 (2001).
12. J. Wang, M. S. Gudiksen, X. Duan, Y. Cui, and C. M. Lieber, *Highly polarized photoluminescence and photodetection from single Indium Phosphide nanowires*. Science **293**, 145 (2001).
13. Y. Huang, X. F. Duan, Y. Cui, L. J. Lauhon, K. H. Kim, and C. M. Lieber**,** *Logic gates and computation from assembled nanowire building blocks*. Science **294**, 1313 (2001).
14. A. Bachtold, P. Hadley, T. Nakanishi, and C. Dekker, *Logic circuits with carbon nanotube transistors*. Science **294**, 1317 (2001).
15. V. Derycke, R. Martel, J. Appenzeller, and P. Avouris, *Carbon nanotube inter- and intramolecular logic gates*. Nano Lett. **1**, 453 (2001).
16. Y. Huang, X. F. Duan, Q. Q. Wei, and C. M. Lieber, *Directed assembly of one-dimensional nanostructures into functional networks*. Science **291**, 630 (2001).
17. T. Rueckes, K. Kim, E. Joselevich, G. Y. Tseng, C. Cheung, and C. M. Lieber, *Carbon nanotubes-based nonvolatile random access memory for molecular computing*. Science **289**, 94 (2000).
18. J. Hu, M. Ouyang, P. Yang, and C. M. Lieber, *Controlled growth and electrical properties of heterojunctions of carbon nanotubes and silicon nanowires.* Nature **399**, 48 (1999).
19. Y. Zhang, T. Ichihashi, E. Landree, F. Nihey, and S. Iijima, *Heterostructures of single-walled carbon nanotubes and carbide nanorods*. Science **285**, 1719 (1999).
20. Y. Y. Wu, R. Fan, and P. D. Yang, *Block-by-block growth of single-crystalline Si/SiGe superlattice nanowires.* Nano Letters **2**, 83 (2002).
21. M. T. Bjork, B. J. Ohlsson, T. Sass, A. I. Persson, C. Thelander, M. H. Magnusson, K. Deppert, L. R. Wallenberg, and L. Samuelson, *One-dimensional steeplechase for electrons realized.* Nano Letters **2**, 87 (2002).
22. M. S. Gudiksen, L. J. Lauhon, J. Wang, D. C. Smith, and C. M. Lieber, *Growth of nanowire superlattice structures for nanoscale photonics and electronics.* Nature **415**, 617 (2002).
23. S. Matsui, *Nanostructure fabrication using electron beam and its application to nanometer devices.* Proceedings of the IEEE **85**, 629 (1997).
24. P. Yang, Y. Wu, and R. Fan, *Inorganic semiconductor nanowires*. Inter. J. Nanoscience **1**, 1 (2002).
25. Y. Zhang and J. Zhu, *Synthesis and characterization of several one-dimensional nanomaterials*. Micron **33**, 523 (2002).
26. G. R. Patzke, F. Krumeich, and R. Nesper, *Oxidic nanotubes and nanorods – anisotropic modules for a future nanotechnology.* Angew. Chem. Int. Ed. **41**, 2446 (2002).
27. S. Matsui, *Nanostructure fabrication using electron beam and its application to nanometer devices.* Proceedings of the IEEE **85**, 629 (1997).
28. Y. Xia, J. A. Rogers, K. E. Paul, and G. M. Whitesides, *Unconventional methods for fabricating and patterning nanostructures*. Chem. Rev. **99***,* 1823 (1999).
29. Y. Chen and A. Pépin, *Nanofabrication: conventional and noncoventional methods*. Electrophoresis **22**, 187 (2001).
30. H. T. Soh, K. W. Guarini, and C. F. Quate, *Scanning probe lithography* (Kluwer, Boston, 2001).
31. T. J. Trentler, K. M. Hickman, S. C. Geol, A. M. Viano, P. C. Gibbons, and W. E. Buhro, *Solution-liquid-solid growth of crystalline III-V semiconductors: an analogy to vapor-liquid-solid growth*. Science **270**, 1791 (1995).
32. X. F. Liu, J. H. Zeng, W. X. Zhang, X. C. Yu, Y. T. Qian, J. B. Cao, and W. Q. Zhang, *Solvothermal route to* Bi_3Se_4 *nanorods at low temperature.* J. Mater. Res. **16**, 3361 (2001).
33. C. M. Lieber, *One-dimensional nanostructures: chemistry, physics and applications.* Solid State Communications **107**, 607 (1998).
34. A. P. Levitt (ed.), *Whisker Technology* (Wiley-Interscience, New York, 1970).
35. C. R. Martin, *Nanomaterials – a membrane-based synthetic approach.* Science **266**, 1961 (1994).
36. D. Al-Mawlawi, C. Z. Liu, and M. Moskovits, *Nanowires formed in anodic oxide nanotemplates*. J. Mater. Res. **9**, 1014 (1994).

37. J. C. Hulteen and C. R. Martin, *A general template-based method for the preparation of nanomaterials.* J. Mater. Chem. **7,** 1075 (1997).
38. N. O. Young and J. Kowal, *Optically active fluorite films.* Nature **183**, 104 (1959).
39. T. Motohiro and Y. Taga, *Thin film retardation plate by oblique deposition.* Appl. Opt. **28**, 2466 (1989).
40. R. M. A. Azzam, *Chiral thin solid films: method of deposition and applications.* Appl. Phys. Lett. **61**, 3118 (1992).
41. K. Robbie, M. J. Brett, and A. Lakhtakia, *Chiral sculptured thin films*. Nature **384**, 616 (1996).
42. K. Robbie, L. J. Friedrich, S. K. Dew, T. Smy, and M. J. Brett, *Fabrication of thin films with highly porous microstructures.* J. Vac. Sci. Technol. A**13**, 1032 (1995).
43. K. Robbie, M. J. Brett, and Akhlesh Lakhtakia, *First thin film realization of a helicoidal bianisotropic medium*. J. Vac. Sci. Technol. A**13**, 2991 (1995).
44. R. Messier, T. Gehrke, C. Frankel, V. C. Venugopal, W. Otaño, and A. Lakhtakia, *Engineered sculptured nematic thin films.* J. Vac. Sci. Technol. A**15**, 2148 (1997).
45. K. Robbie and M. J. Brett, *Sculptured thin films and glancing angle deposition: growth mechanisms and applications.* J. Vac. Sci. Technol. A**15**, 1460 (1997).
46. K. Robbie, J. C. Sit, and M. J. Brett, *Advanced techniques for glancing angle deposition.* J. Vac. Sci. Technol. A**16**, 1115 (1998).
47. F. Liu, M. T. Umlor, L. Shen, J. Weston, W. Eads, J. A. Barnard, and G. J. Mankey, *The growth of nanoscale structured iron films by glancing angle deposition.* J. Appl. Phys. **85**, 5486 (1999).
48. R. Messier, V. C. Venugopal, and P. D. Sunal, *Origin and evolution of sculptured thin films.* J. Vac. Sci. Technol. A**18**, 1538 (2000).
49. M. Malac and R. F. Egerton, *Observations of the microscopic growth mechanism of pillars and helices formed by glancing-angle thin-film deposition.* J. Vac. Sci. Technol. A**19**, 158 (2001).
50. M. Malac, R. F. Egerton, M. J. Brett, and B. Dick, *Fabrication of submicrometer regular arrays of pillars and helices.* J. Vac. Sci. Technol. B**17**, 2671 (1999).
51. M. Malac, R. F. Egerton, and M. Brett, *Thin film deposited at glancing incident and their applications.* Vacuum Technol. & Coating, July, 48 (2001).
52. Y.-P. Zhao, D.-X. Ye, G.-C. Wang, and T.-M. Lu, *Sculpture aligned nano-column arrays and nano-flowers by glancing angle deposition.* Nano Letters **2**, 351 (2002).
53. Y.-P. Zhao, D.-X. Ye, P.-I. Wang, G.-C. Wang, and T.-M. Lu, *Fabrication Si nano-columns and square springs on self-assembly colloid substrates*. International Journal of Nanoscience **1**, 87 (2002).
54. D.-X. Ye, Y.-P. Zhao, G.-R. Yang, Y.-G. Zhao, G.-C. Wang, and T.-M. Lu, *Manipulating the column tilt angles of nanocolumnar films by glancing angle deposition.* Nanotechnology **13**, 615 (2002).
55. A. Lisfi and J.C. Lodder, *Magnetic domains in Co thin films obliquely sputtered on a polymer substrate.* Phys. Rev. B **63**, 174441 (2001).
56. J. M. Nieuwenhuizen and H. B. Haanstra, *Microfractography of thin films.* Philips Tech. Rev. **27**, 87 (1966).
57. R. N. Trait, T. Smy, and M. J. Brett, *Modeling and characterization of columnar growth in evaporated-films.* Thin Solid Films **226**, 196 (1993).
58. R. Micheletto, H. Fukuda, and M. Ohtsu, *A simple method for the production of a two-dimensional ordered array of small latex particles.* Langmuir **11**, 3333 (1995).